EPIGENETICS

Highly enriched BEND3 prevents the premature activation of bivalent genes during differentiation

Jing Zhang[1]†, Yan Zhang[1]†, Qinglong You[1,2]†, Chang Huang[1], Tiantian Zhang[1], Mingzhu Wang[3], Tianwei Zhang[1], Xiaocheng Yang[1,2], Jun Xiong[1], Yingfeng Li[1], Chao-Pei Liu[1], Zhuqiang Zhang[1], Rui-Ming Xu[1,2]*, Bing Zhu[1,2]*

Bivalent genes are ready for activation upon the arrival of developmental cues. Here, we report that BEND3 is a CpG island (CGI)–binding protein that is enriched at regulatory elements. The cocrystal structure of BEND3 in complex with its target DNA reveals the structural basis for its DNA methylation–sensitive binding property. Mouse embryos ablated of *Bend3* died at the pregastrulation stage. *Bend3* null embryonic stem cells (ESCs) exhibited severe defects in differentiation, during which hundreds of CGI-containing bivalent genes were prematurely activated. BEND3 is required for the stable association of polycomb repressive complex 2 (PRC2) at bivalent genes that are highly occupied by BEND3, which suggests a reining function of BEND3 in maintaining high levels of H3K27me3 at these bivalent genes in ESCs to prevent their premature activation in the forthcoming developmental stage.

CpG islands (CGIs) are generally associated with housekeeping genes (*1*–*3*). BANP, a DNA methylation–sensitive CGI-binding protein, is required for their activation (*4*). CGIs are also associated with bivalent genes (*5*, *6*), so we investigated whether and how CGI-associated bivalent genes are regulated by sequence-specific recognition.

BEND3 was identified as an unmethylated DNA–binding protein in vitro (*7*, *8*). Chromatin immunoprecipitation sequencing (ChIP-seq) experiments in mouse TT2 embryonic stem cells (ESCs) (*9*) identified a total of 27,536 BEND3 peaks, with ~51 and 28% of them overlapped with promoters and enhancers, respectively (Fig. 1A).

BEND3 occupancy was heavily biased toward CGI-associated genes (Fig. 1, B to D). Approximately 85% (12,037 of 14,117) of CGI-associated transcription start sites (TSSs) and 81% of CGI-associated enhancers (1246 of 1533) were bound by BEND3 (Fig. 1, C and D). BEND3 and nonmethylated island (NMI) signals (*10*) displayed a strong overlap at BEND3 peaks (fig. S1A). Notably, BEND3 occupied active (H3K4me3 only) and bivalent promoters (H3K4me3 and H3K27me3) but not silenced promoters (H3K27me3 only) (Fig. 1E). At enhancers, BEND3 preferentially occupied poised enhancers marked by H3K4me1 and H3K27me3 (Fig. 1F). Notably, 45% of poised enhancer–associated genes are bivalent genes (Fig. 1G) (*11*–*13*).

[1]National Laboratory of Biomacromolecules, CAS Center for Excellence in Biomacromolecules, Institute of Biophysics, Chinese Academy of Sciences, Beijing 100101, China. [2]College of Life Sciences, University of Chinese Academy of Sciences, Beijing 100049, China. [3]Institutes of Physical Science and Information Technology, Anhui University, Hefei 230601, Anhui, China.
***Corresponding author. Email: rmxu@ibp.ac.cn (R.-M.X.); zhubing@ibp.ac.cn (B.Z.)**
†These authors contributed equally to this work.

A sequence motif (CCCACGCG) containing two CpG sites (Fig. 2A) was identified as the most enriched motif using the ChIP-seq analysis software HOMER (*14*). BEND3-bound regions exhibited far lower CpG methylation levels than those at the unbound sites (Fig. 2B).

The binding motif of BANP shares CGCG with the BEND3 motif but differs at flanking regions (Fig. 2A). BANP is enriched at the CGI promoters but not at the CGI enhancers (fig. S1B) (*4*). Different from BEND3, BANP strongly prefers the active CGI promoters (fig. S1C), which suggests that BEND3 may play a distinct role in regulating bivalent genes.

BEND3 has four BEN domains (fig. S2A), and the *Drosophila* Insv BEN domain is a sequence-specific DNA-binding module (*15*). In electrophoretic mobility shift assays (EMSAs), only the fourth BEN domain (BEN4) of BEND3 exhibited binding toward a probe containing the CCCACGCG motif (Fig. 2C).

To understand how BEN4 recognizes its target DNA in a DNA methylation–sensitive manner, we solved a 2.5-Å structure of a selenomethionine-substituted L740→M (L740M) mutant of BEN4 bound to a 16-nucleotide oligomer DNA containing the consensus recognition motif and a 3.5-Å structure of native BEN4 bound to the same DNA. Both structures show a domain-swapped dimer of BEN4 bound to two independent DNA duplexes, with the L740M dimer generated by crystal symmetry (Fig. 2D). Despite the difference in the relative orientation of two protein-DNA modules within each complex and variation in the hinge region connecting the two globular domains, the two structures share a common DNA-binding mode (fig. S2B). We will use the more accurate L740M structure for description henceforth, unless otherwise specified. Each BEN4 monomer features five α helices, α1 to α5, and an independent DNA-binding module in BEN4 is formed by α1 to α4 from one monomer and a domain-swapped α5′ from the neighboring molecule (Fig. 2D). By contrast, the third BEN domain (BEN3) is monomeric in solution and in the crystal (fig. S2C). BEN3 shares high sequence similarity with BEN4 (fig. S2D), and the overall structure of the BEN3 domain is very similar to that of BEN4 except for the orientation of α5, which folds back and packs against its N-terminal helices to form a globular domain (fig. S2C). The monomeric BEN3 structure offers insights into the mechanism of dimer formation of BEN4. The dimeric conformation of BEN4 is mediated by its hinge region between α4 and α5 (Fig. 2D). A monomeric BEN4 mutant (BEN4-mu) with its hinge region (residues 787 to 792) replaced by the counterpart sequence of BEN3 (residues 621 to 626) can still bind to the consensus motif, but only one DNA molecule can be bound (fig. S2E).

The BEN4 domain interacts with both strands of DNA, with α5 (residues 791 to 818) occupying the major groove and a segment of the loop between α3 and α4 (residues 756 to 771) contacting the minor groove. Detailed protein-DNA contacts involving the consensus sequence are illustrated schematically (Fig. 2E). For the top strand, E804 and C(+7) form a key base-specific contact, whereas R808, S732, and N735 contact the sugar-phosphate backbone. For the bottom strand, key base-specific contacts include that between R807 and G(−9) and that between K812 and G(−5) and G(−6), whereas the N759, S761, K766, H795, and K813 contact the sugar-phosphate backbone. Notably, the side chains of E804, R807, and K812 on α5 form base-specific hydrogen bonds in the major groove (Fig. 2F). Mutations of R807 or K812 abolished the DNA-binding activity of BEN4 (Fig. 2G). Moreover, in *Bend3* knockout (KO) ESCs rescued by a full-length BEND3 R807K-K812E mutant (fig. S2F), the chromatin localization of BEND3 was mostly lost (Fig. 2H), which indicates that BEN4 is the main domain responsible for chromatin localization. We observed a close contact between the guanidino group of R807 and C(−10). Modeling of a 5′-methyl (5′-m) group onto C(−10) introduces a direct clash between 5′-mC(−10) and R807 (Fig. 2I). This is in accordance with the observation that methylation at C(−10) prevented BEN4 from binding its target DNA (Fig. 2J). Within the CCCACGCG motif, only the first six base pairs are required for base-specific interaction or methylation-sensitive binding to BEND3.

We acquired *Bend3*$^{+/tm1a}$ mice carrying a recombinant *Bend3*^{tm1a} allele with an IRES:LacZ trapping cassette inserted into the third intron (fig. S3A) (*16*). A *Bend3*$^{-}$ allele with all four BEN domains excised was obtained after crossing with *Zp3-Cre* mice.

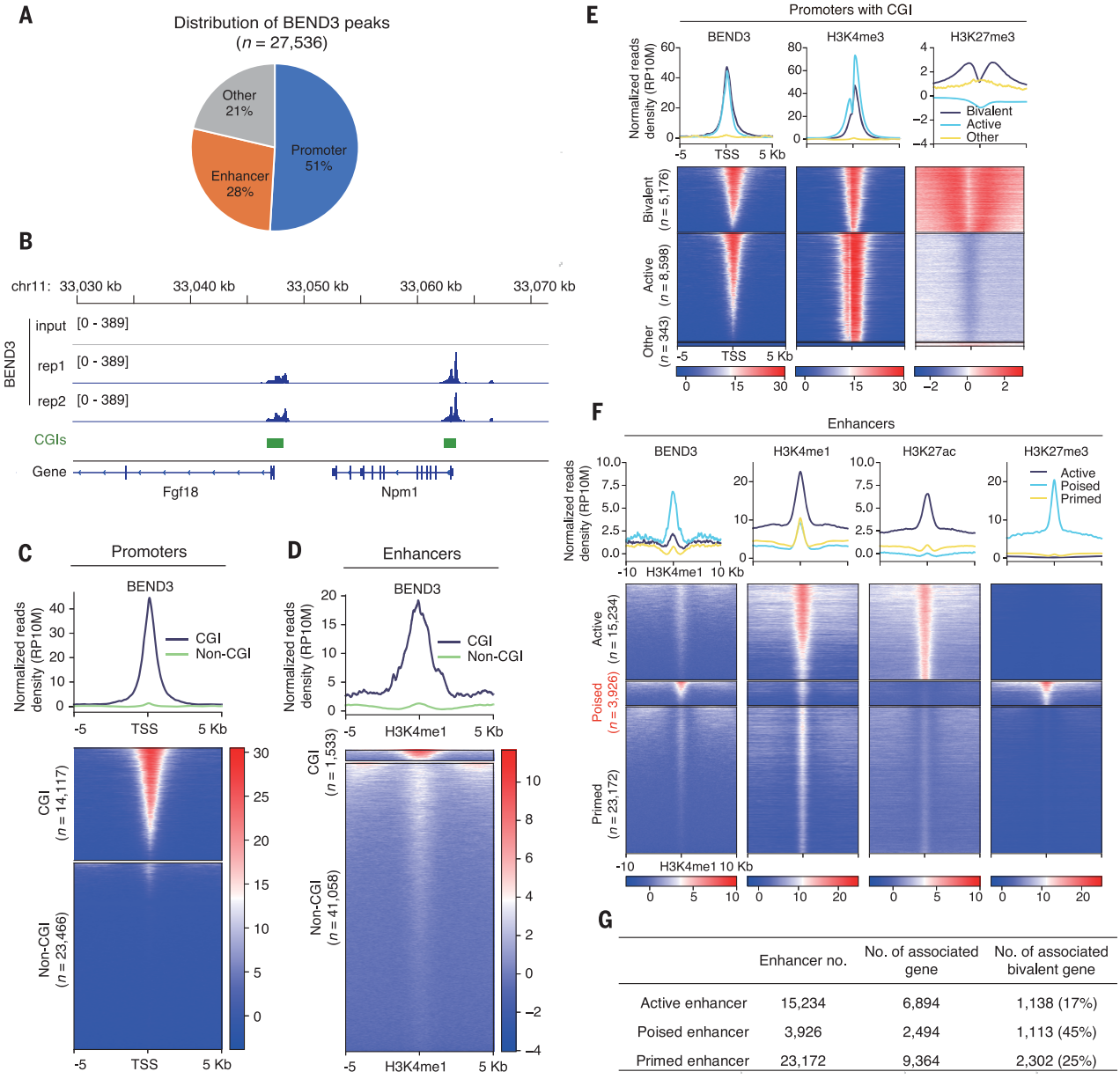

Fig. 1. BEND3 is enriched at CGI promoters and CGI enhancers. (**A**) Distribution of BEND3 ChIP-seq peaks. (**B**) Examples of BEND3 ChIP-seq tracks. chr11, chromosome 11. (**C**) Heatmaps of BEND3 ChIP-seq signals around the TSSs of CGI and non-CGI promoters. (**D**) Heatmaps of BEND3 ChIP-seq signals surrounding CGI and non-CGI enhancers. (**E**) Heatmaps of BEND3 ChIP-seq signals around the TSSs of different types of CGI promoters. (**F**) Heatmaps of BEND3 ChIP-seq signals surrounding different types of enhancers. (**G**) The total number of enhancers in each group and the number and percentage of their associated bivalent genes.

After crossing *Bend3*$^{+/-}$ males and females, no *Bend3*$^{-/-}$ pups were born and no *Bend3*$^{-/-}$ embryos were identified at embryonic day 6.5 (E6.5); however, *Bend3*$^{-/-}$ embryos were observed at around the Mendelian ratio at E3.5 (Fig. 3A), which suggests that *Bend3* deletion led to embryonic lethality between E3.5 and E6.5. We derived *Bend3*$^{+/+}$ [wild-type (WT)], *Bend3*$^{+/-}$ (*Bend3* Het), and *Bend3*$^{-/-}$ (*Bend3* KO) ESCs from corresponding blastocysts (Fig. 3B and fig. S3B). *Bend3* KO ESCs appeared to be largely normal in morphology, alkaline phosphatase staining, and expression of self-renewal genes (fig. S3, C to E).

Given the pregastrulation lethal phenotype, BEND3 is likely required for ESC differentiation. In fact, 1×10^6 *Bend3* KO ESCs injected into the groins of immune-deficient mice could not form teratomas (Fig. 3C). Next, we performed embryoid body (EB) formation assay. After hanging drop culture for 2 days, EBs derived from *Bend3* KO ESCs were smaller and gradually shrank as a result of massive cell death (Fig. 3D), which again indicates a critical role of BEND3 in differentiation.

To clarify the molecular mechanism underlying the differentiation defect, we harvested WT, *Bend3* Het, and *Bend3* KO EBs at day 1 (d1), d2, and d3 during differentiation and performed RNA sequencing (RNA-seq) experiments. Principal components analysis (PCA) revealed that the expression profiles of *Bend3* KO cells gradually differed from the control cells during differentiation (Fig. 4A), and the number of dysregulated genes gradually increased as differentiation progressed (Fig. 4B); however, even at d3, only a fraction of BEND3 targets were dysregulated. We noticed that a

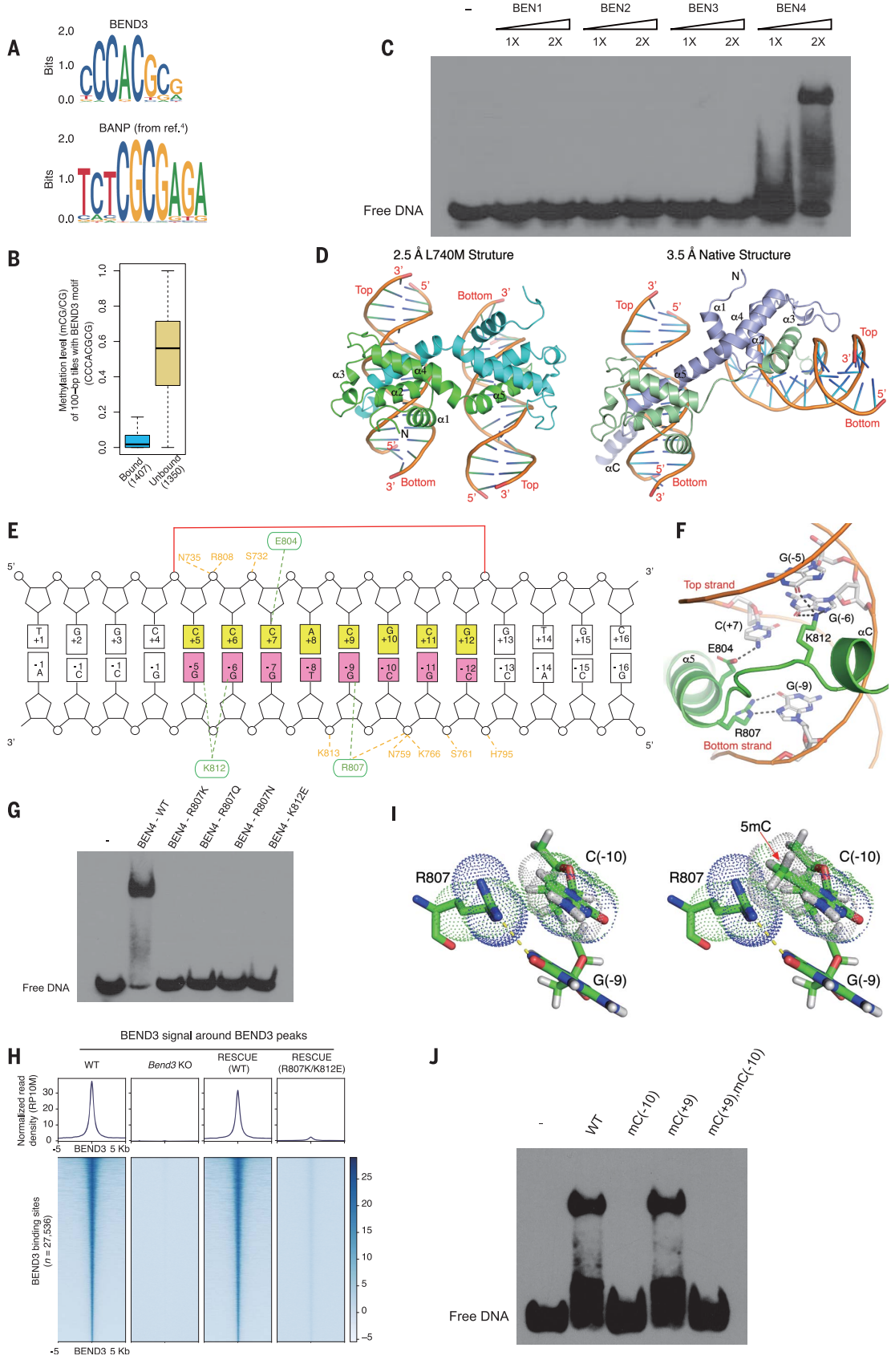

Fig. 2. Sequence-specific recognition of BEND3 and the underlying structure basis. (**A**) Top BEND3-binding motif identified by HOMER (top), and the BANP-binding motif from literature (*4*) (bottom). (**B**) DNA methylation level of BEND3-bound and BEND3-unbound 100–base pair (bp) tiles containing BEND3-binding motif. (**C**) EMSA results of the binding of individual recombinant BEN domain with a 16-nucleotide oligomer DNA probe containing BEND3-binding motif. Proteins were added with increasing amount. (**D**) Structures of the complex containing two BEN4 domains bound to two 16-nucleotide oligomer DNA duplexes. (**E**) A schematic drawing of BEN4-DNA interaction. (**F**) A detailed view of BEN4-DNA interaction. (**G**) EMSA results with BEN4 wild types or mutants. (**H**) Heatmaps of BEND3 ChIP-seq signals around BEND3-binding sites in WT TT2, *Bend3* KO, and rescued cell lines. (**I**) Structural explanation for the DNA methylation–sensitive property of BEN4. (**J**) EMSA results showing methylation at C(−10) blocks BEN4 binding. Single-letter abbreviations for the amino acid residues are as follows: A, Ala; C, Cys; D, Asp; E, Glu; F, Phe; G, Gly; H, His; I, Ile; K, Lys; L, Leu; M, Met; N, Asn; P, Pro; Q, Gln; R, Arg; S, Ser; T, Thr; V, Val; W, Trp; and Y, Tyr.

A

Stage	*Bend3* $^{+/+}$	*Bend3* $^{+/-}$	*Bend3* $^{-/-}$	Total
Postnatal	28	42	0	70
E6.5	9	16	0	25
E3.5	11	22	8	41

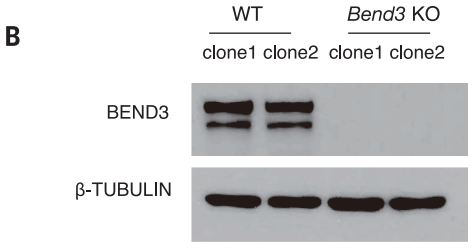

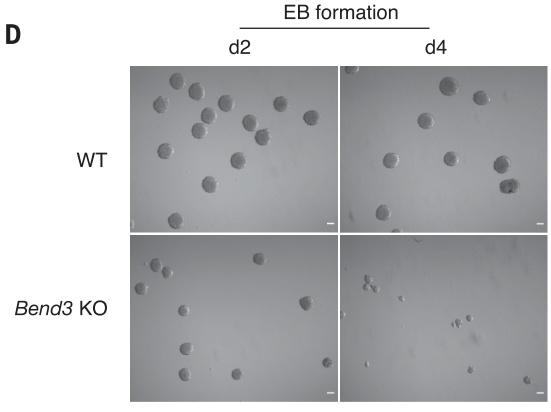

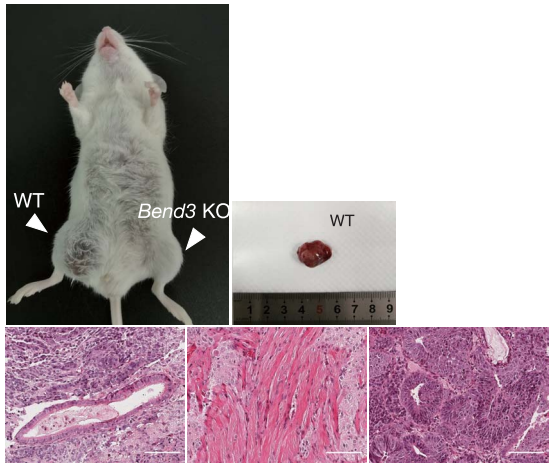

Left	Tumor (mm)	Right	Tumor (mm)
WT clone1	15.2X11.3X8.2	*Bend3* KO clone2	-
WT clone2	6.1X7.0X5.1	*Bend3* KO clone2	-
Bend3 Het clone1	16.9X20.3X16.6	*Bend3* KO clone2	-
Bend3 Het clone2	18.5X19.8X12	*Bend3* KO clone2	-
Bend3 KO clone1	-	WT clone1	17X11.6X8.9
Bend3 KO clone1	-	WT clone2	13.4X9.8X6.0
Bend3 KO clone1	-	*Bend3* Het clone1	15.2X13.5X9.42
Bend3 KO clone1	-	*Bend3* Het clone2	10.8X10.1X7.6

Fig. 3. BEND3 is indispensable for development and differentiation. (**A**) Genotypes of littermates of *Bend3*$^{+/-}$ intercrosses at indicated stages. (**B**) Western blotting of whole-cell lysates from indicated ESC clones. (**C**) Teratoma assay of WT, *Bend3* Het, and *Bend3* KO ESCs in SCID (severe combined immunodeficient) mice. (Top) Teratomas formed by WT and *Bend3* KO ESCs. (Middle) Hematoxylin and eosin (H&E) staining of teratoma from WT ESCs. (Bottom) Sizes of the teratomas after 4-week subcutaneous injection to the left or right groin of SCID mice with indicated ESCs. (**D**) Representative images showing the morphologies of EBs from WT and *Bend3* KO ESCs at d2 and d4 of differentiation. Scale bars, 100 μm.

small group of BEND3 peaks (~5%) exhibited much greater levels of BEND3 signal (Fig. 4C), and they tended to have more BEND3-binding motifs (Fig. 4D). BEND3 is associated with both active and bivalent genes (Fig. 1E). However, gene set enrichment analysis (GSEA) results indicated that bivalent genes that were associated with high levels of BEND3—but not their counterparts among the active genes—were significantly up-regulated in *Bend3* KO EBs at d3 (fig. S4A). These data suggest that BEND3 preferentially attenuates the expression of its top target bivalent genes during differentiation.

To analyze the effect of BEND3 binding on gene expression, we categorized bivalent and active BEND3 target genes according to the number of BEND3-binding motifs (≥5, 3 to 4, 1 to 2, or 0) of their associated BEND3 peaks and plotted their transcriptional changes upon *Bend3* deletion. Bivalent BEND3 targets with the highest number of BEND3 motifs were up-regulated upon differentiation in *Bend3* KO EBs at d2 and d3, but such a trend was not observed in ESCs or for the active target genes (Fig. 4E and fig. S4, B and C).

Notably, the aberrantly up-regulated genes tended to exhibit some degree of up-regulation in d2 and d3 WT EBs compared with WT ESCs (fig. S4D). We speculated that these genes might be up-regulated during normal differentiation, and the loss of BEND3 accelerated this process. To test this, we performed further analysis using a long-term differentiation (up to d8) dataset from WT J1 ESCs. We focused on BEND3 targets that were bivalent and were aberrantly up-regulated in *Bend3* KO d3 EBs, and we found that these genes were not up-regulated at d2 but were robustly activated at d5 and d8 in WT EBs (fig. S4E). Compared with WT ESCs, only 4% of these genes were up-regulated in WT d2 EBs, but 23 and 43% of them became up-regulated in WT d5 and d8 EBs, respectively (Fig. 4F).

BEND3 participates in the recruitment of PRC2 to major satellites in cells lacking DNA methylation (*17*), and BEND3 interacts with the NuRD complex (*17*, *18*). Therefore, we performed ChIP-seq experiments for SUZ12 (a subunit of PRC2) and CHD4 (a subunit of NuRD) in WT and *Bend3* KO ESCs. We found that the SUZ12 signal at the BEND3 peaks was reduced upon the loss of BEND3, the levels of SUZ12 decreased, and the concomitant H3K27me3 reduction correlated with the number of BEND3-binding motifs (Fig. 4, G and H, and fig. S5A). These changes were specific for bivalent targets, especially those that were aberrantly up-regulated in d3 *Bend3* KO EBs, but not for active targets (fig. S5, B and C). We did not observe a loss of CHD4 occupancy or an increase of assay for transposase-accessible chromatin with high-throughput sequencing (ATAC-seq) signal upon *Bend3* deletion, although the increase of H3K27ac accompanied the loss of H3K27me3 (Fig. 4G and fig. S5A).

We next analyzed the expression of genes associated with all of the H3K27me3 peaks that overlapped with BEND3 peaks and exhibited greater than twofold reduction of H3K27me3 signal upon *Bend3* deletion. We found that the loss of H3K27me3 did not lead

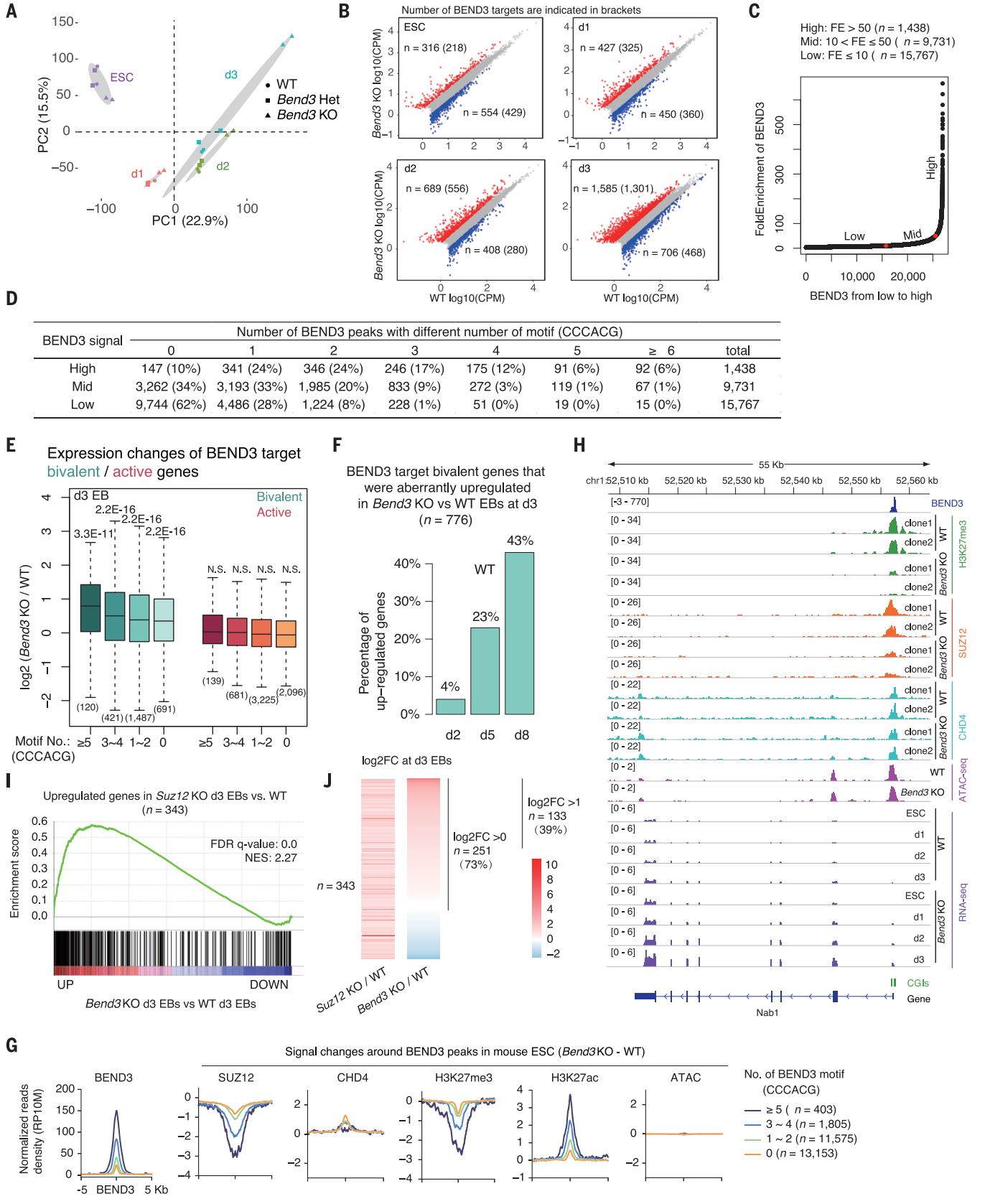

BEND3 signal	Number of BEND3 peaks with different number of motif (CCCACG)							
	0	1	2	3	4	5	≥ 6	total
High	147 (10%)	341 (24%)	346 (24%)	246 (17%)	175 (12%)	91 (6%)	92 (6%)	1,438
Mid	3,262 (34%)	3,193 (33%)	1,985 (20%)	833 (9%)	272 (3%)	119 (1%)	67 (1%)	9,731
Low	9,744 (62%)	4,486 (28%)	1,224 (8%)	228 (1%)	51 (0%)	19 (0%)	15 (0%)	15,767

Fig. 4. *Bend3* deletion leads to premature activation of highly occupied bivalent genes during differentiation. (**A**) PCA results of transcriptomes in WT, *Bend3* Het, and *Bend3* KO ESCs and EBs at d1, d2, and d3. Two clones were used for each genotype. (**B**) Scatter plots showing gene expression levels between WT and *Bend3* KO ESCs and EBs at d1, d2, and d3 during differentiation. Significantly dysregulated (fold change > 2; adjusted $P < 0.05$

and $P < 0.01$) genes are labeled in red (up-regulated) or blue (down-regulated). Other genes are labeled in gray. (**C**) Scatter plot showing the fold enrichment (FE) of all BEND3 ChIP-seq peaks (n = 26,936) identified in WT ESCs. (**D**) Number and percentage of all BEND3 ChIP-seq peaks containing different number of motif (CCCACG). (**E**) Box plots showing the transcriptional changes of BEND3 target bivalent and active genes in d3 EBs. Genes are grouped by the motif number of associated BEND3 peaks at promoters or enhancers, and genes with a read count of >50 in at least one sample of a comparison were kept for analysis. (**F**) Percentage of up-regulated genes in d2, d5, and d8 EBs from J1 ESCs for aberrantly up-regulated BEND3 target bivalent genes in *Bend3* KO d3 EBs. (**G**) Changes of normalized read density of SUZ12, CHD4, H3K27me3, H3K27ac, and chromatin accessibility (ATAC-seq) at four BEND3 peak groups in WT and *Bend3* KO mouse ESCs. (**H**) Snapshots of a representative region strongly occupied by BEND3 showing indicated chromatin features and expression levels. (**I**) GSEA for up-regulated genes in *Suz12* KO d3 EBs with respect to the global transcriptional changes observed in *Bend3* KO d3 EBs. (**J**) The effect of *Bend3* KO on the expression of genes up-regulated in *Suz12* KO d3 EBs. log2FC, $\log_2$ fold change.

to immediate activation of these genes in ESCs but caused premature up-regulation during differentiation (fig. S5D).

Finally, we analyzed public transcriptome data from WT and *Suz12* KO EBs (*19*). GSEA results indicated that genes up-regulated in *Suz12* KO d3 EBs were significantly enriched in genes up-regulated in *Bend3* KO d3 EBs (Fig. 4I). Among 343 genes with greater than twofold up-regulation in *Suz12* KO d3 EBs, 73% (251) of them exhibited increased expression, and 39% (133) of them reached the twofold threshold in *Bend3* KO d3 EBs (Fig. 4J). These results provide further support that BEND3 function is largely PRC2 dependent.

Taken together, our results suggest that BEND3 is required for the optimal association of PRC2 at bivalent CGIs highly enriched with BEND3. *Bend3* deletion leads to reduced PRC2 and H3K27me3 levels at these genes. This does not immediately activate most of these genes because the differentiation signal and corresponding transcription factors are not yet available; however, the loss of H3K27me3 affects the kinetics of bivalent gene induction upon the arrival of the differentiation signal and causes premature activation and the failure of differentiation. Gene bivalency was observed many years ago (*20*), but its exact function remains a matter of debate. It is widely expected in priming bivalent genes for faster induction, largely because of the enrichment of H3K4me3. However, MLL2 deletion abolishes H3K4me3 at bivalent genes without affecting their induction kinetics (*21*). We propose that gene bivalency can prevent premature gene activation during differentiation—an opposite effect of priming—which we refer to as reining.

Not all BEND3 targets are equally affected by *Bend3* deletion, and similar events have been observed for many sequence-specific binding proteins (*22*–*24*), likely because of the compounding effect of other sequence-specific binding proteins nearby. Nevertheless, the finding that BEND3 has a stronger effect at its highly occupied targets is notable and reflects a principle coined as "more is different" (*25*).

REFERENCES AND NOTES

1. F. Larsen, G. Gundersen, R. Lopez, H. Prydz, *Genomics* **13**, 1095–1107 (1992).
2. J. Zhu, F. He, S. Hu, J. Yu, *Trends Genet.* **24**, 481–484 (2008).
3. S. Beck *et al.*, *Nat. Commun.* **5**, 5490 (2014).
4. R. S. Grand *et al.*, *Nature* **596**, 133–137 (2021).
5. T. S. Mikkelsen *et al.*, *Nature* **448**, 553–560 (2007).
6. M. Ku *et al.*, *PLOS Genet.* **4**, e1000242 (2008).
7. J. Xiong *et al.*, *Mol. Cell* **64**, 913–925 (2016).
8. M. Iurlaro *et al.*, *Genome Biol.* **14**, R119 (2013).
9. M. Tachibana *et al.*, *Genes Dev.* **16**, 1779–1791 (2002).
10. H. K. Long *et al.*, *eLife* **2**, e00348 (2013).
11. E. Blanco, M. González-Ramírez, A. Alcaine-Colet, S. Aranda, L. Di Croce, *Trends Genet.* **36**, 118–131 (2020).
12. A. Rada-Iglesias *et al.*, *Nature* **470**, 279–283 (2011).
13. S. Cruz-Molina *et al.*, *Cell Stem Cell* **20**, 689–705.e9 (2017).
14. S. Heinz *et al.*, *Mol. Cell* **38**, 576–589 (2010).
15. Q. Dai *et al.*, *Genes Dev.* **27**, 602–614 (2013).
16. M. C. Birling *et al.*, *Nat. Genet.* **53**, 416–419 (2021).
17. N. Saksouk *et al.*, *Mol. Cell* **56**, 580–594 (2014).
18. K. M. Sathyan, Z. Shen, V. Tripathi, K. V. Prasanth, S. G. Prasanth, *J. Cell Sci.* **124**, 3149–3163 (2011).
19. E. M. Riising *et al.*, *Mol. Cell* **55**, 347–360 (2014).
20. B. E. Bernstein *et al.*, *Cell* **125**, 315–326 (2006).
21. D. Hu *et al.*, *Nat. Struct. Mol. Biol.* **20**, 1093–1097 (2013).
22. D. A. Cusanovich, B. Pavlovic, J. K. Pritchard, Y. Gilad, *PLOS Genet.* **10**, e1004226 (2014).
23. D. Kenzelmann Broz *et al.*, *Genes Dev.* **27**, 1016–1031 (2013).
24. F. Spitz, E. E. Furlong, *Nat. Rev. Genet.* **13**, 613–626 (2012).
25. P. W. Anderson, *Science* **177**, 393–396 (1972).

ACKNOWLEDGMENTS

We thank the staff from the animal center of the Institute of Biophysics for technical assistance. We thank X. Yang and J. Hao from the Pathology Analysis Group of the Institute of Biophysics for assistance with paraffin embedding and histomorphology. We thank beamline scientists at BL17U of the Shanghai Synchrotron Radiation Facility (SSRF) for technical support during data collection. **Funding:** This work was supported by grants from the Chinese Ministry of Science and Technology (2019YFA0801401, 2017YFA0504100, 2019YFA0508900, 2017YFA0504202, and 2016YFA0100400), the China Natural Science Foundation (31771429, 31501059, 31991162, and 31521002), the Chinese Academy of Sciences (XDB37010100, XDB39010100, and QYZDY-SSW-SMC031), and the K. C. Wong educational foundation (GJTD-2020-06). Z.Z. and J.X. are supported by the Youth Innovation Promotion Association (2017133 and 2020097) of the Chinese Academy of Sciences. **Author contributions:** B.Z. and R.-M.X. designed and supervised the project. J.Z. performed most of the experiments. Y.Z. performed the bioinformatics analysis. Q.Y. performed the crystallization experiments. C.H., Tiant.Z., M.W., Tianw.Z., J.X., X.Y., Y.L., C.-P. L., and Z.Z. assisted in experiments and data analysis. J.Z., Y.Z., Q.Y., R.-M.X., and B.Z. wrote the manuscript, and all the authors read and commented on the manuscript. **Competing interests:** The authors declare no competing interests. **Data and materials availability:** The ChIP-seq, CUT&Tag (cleavage under targets and tagmentation), RNA-seq, ATAC-seq, and T-WGBS datasets have been deposited in BIG GSA (under accession no. CRA004815 and publicly accessible at https://ngdc.cncb.ac.cn/gsa). Atomic coordinates and x-ray diffraction data have been deposited in the Protein Data Bank under the accession codes 7V9F, 7V9G, 7V9H, and 7V9I for the BEN4 L740M and native, BEN3, and BEN4-mu structures, respectively. Materials generated in this study will be provided upon request.

SUPPLEMENTARY MATERIALS

science.org/doi/10.1126/science.abm0730
Materials and Methods
Figs. S1 to S7
Tables S1 to S3
References (*26*–*52*)
MDAR Reproducibility Checklist

View/request a protocol for this paper from *Bio-protocol*.

26 August 2021; accepted 2 February 2022
Published online 10 February 2022
10.1126/science.abm0730